

Title	Solid-state synthesis of embedded single-crystal metal oxide and phosphate nanoparticles and in situ crystallization
Authors	Díaz, Carlos;Valenzuela, María Luisa;Bravo, Daniel;Dickinson, Calum;O'Dwyer, Colm
Publication date	2011-05-30
Original Citation	Diaz, C., Valenzuela, M. L., Bravo, D., Dickinson, C. and O'Dwyer, C. (2011) 'Solid-state synthesis of embedded single-crystal metal oxide and phosphate nanoparticles and in situ crystallization', Journal of Colloid and Interface Science, 362(1), pp. 21-32. http://www.sciencedirect.com/science/article/pii/S0021979711006461
Type of publication	Article (peer-reviewed)
Link to publisher's version	10.1016/j.jcis.2011.05.066
Rights	© 2011 Elsevier Inc. This manuscript version is made available under the CC-BY-NC-ND 4.0 license - http://creativecommons.org/licenses/by-nc-nd/4.0/
Download date	2024-05-01 18:44:59
Item downloaded from	https://hdl.handle.net/10468/2814

Accepted Manuscript

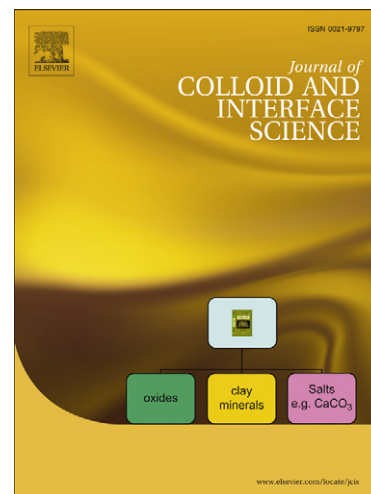
Solid-State Synthesis of Embedded Single-Crystal Metal Oxide and Phosphate Nanoparticles and In-Situ Crystallization

C. Díaz, M.L. Valenzuela, D. Bravo, C. Dickinson, C. O'Dwyer

PII: S0021-9797(11)00646-1
DOI: [10.1016/j.jcis.2011.05.066](https://doi.org/10.1016/j.jcis.2011.05.066)
Reference: YJCIS 16960

To appear in: *Journal of Colloid and Interface Science*

Received Date: 28 January 2011
Accepted Date: 20 May 2011



Please cite this article as: C. Díaz, M.L. Valenzuela, D. Bravo, C. Dickinson, C. O'Dwyer, Solid-State Synthesis of Embedded Single-Crystal Metal Oxide and Phosphate Nanoparticles and In-Situ Crystallization, *Journal of Colloid and Interface Science* (2011), doi: [10.1016/j.jcis.2011.05.066](https://doi.org/10.1016/j.jcis.2011.05.066)

This is a PDF file of an unedited manuscript that has been accepted for publication. As a service to our customers we are providing this early version of the manuscript. The manuscript will undergo copyediting, typesetting, and review of the resulting proof before it is published in its final form. Please note that during the production process errors may be discovered which could affect the content, and all legal disclaimers that apply to the journal pertain.

Solid-State Synthesis of Embedded Single-Crystal Metal Oxide and Phosphate Nanoparticles and In-Situ Crystallization

C. Díaz,^{a,*} M. L. Valenzuela,^b D. Bravo,^a C. Dickinson,^c and C. O'Dwyer^{c,d,†}

^a*Departamento de Química, Facultad de Ciencias, Universidad de Chile, Las Palmeras 3425, Santiago, Chile*

^b*Universidad Andres Bello, Departamento de Ciencias Químicas, Facultad de Ecología y Recursos Naturales, Av. Republica 275, Santiago, Chile*

^c*Materials and Surface Science Institute, University of Limerick, Limerick, Ireland*

^d*Department of Physics and Energy, University of Limerick, Limerick, Ireland*

* E-mail: cdiaz@uchile.cl; Tel: +56 2 9787367

† E-mail: colm.odwyer@ul.ie; Tel: +353 61 202288

Abstract

A new solid state organometallic route to embedded nanoparticle-containing inorganic materials is shown, through pyrolysis of metal-containing derivatives of cyclotriphosphazenes. Pyrolysis in air and at 800 °C of new molecular precursors gives individual single-crystal nanoparticles of SiP_2O_7 , TiO_2 , P_4O_7 , WP_2O_7 and SiO_2 , depending on the precursor used. High resolution transmission electron microscopy investigations reveal, in most cases, perfect single crystals of metal oxides and the first nanostructures of negative thermal expansion metal phosphates with diameters in the range 2-6 nm for all products. While all nanoparticles are new by this method, WP_2O_7 and SiP_2O_7 nanoparticles are reported for the first time. *In-situ* recrystallization formation of nanocrystals of SiP_2O_7 was also observed due to electron beam induced reactions during measurements of the nanoparticulate pyrolytic products SiO_2 and P_4O_7 . The possible mechanism for the formation of the nanoparticles at much lower temperatures than their bulk counterparts in both cases is discussed. Degrees of stabilization from the formation of P_4O_7 affects the nanocrystalline products: nanoparticles are observed for WP_2O_7 , with coalescing crystallization occurring for the amorphous host in which SiP_2O_7 crystals form as a solid within a solid. The approach allows the simple formation of multimetallic, monometallic, metal-oxide and metal phosphate nanocrystals embedded in an amorphous dielectric. The method and can be extended to nearly any metal capable of successful coordination as an organometallic to allow embedded nanoparticle layers and features to be deposited or written on surfaces for application as high mobility pyrophosphate lithium-ion cathode materials, catalysis and nanocrystal embedded dielectric layers.

1. Introduction

Chemical reactions at nanoscale level are of increasing interest from many standpoints.^[1-4] Organometallic approaches have been shown to be generalized to several metal oxides from semiconducting to magnetic materials as well as from monometallic to mixed-metal-oxide nanomaterials. Control over size, shape, size distribution and surface state is very important and the rational preparation of nanoparticles has wide implications from a fundamental point of view and also for applications. The high surface areas exhibited by nanoparticles produce intrinsically high surface reactivities allowing surface reactions to approach stoichiometric conversions.^[5] Metal oxides exhibit fascinating electronic and magnetic properties including metallic, insulating or semiconducting and ferro-, ferri-, or antiferromagnetic behavior.^[6] Some oxides possess ferroelectric or piezoelectric properties, some others are superconducting, or exhibit colossal magnetoresistance. Many examples of metal-oxide nanostructure application include catalysis, sensing, magnetic recording media, and energy storage/conversion have been recently discussed.^[7]

Chemical techniques are widely used to produce nanostructured materials due to their straightforward nature and the potential for producing large quantities of the final product. Methods such as chemical and physical vapour deposition, oxidation or condensation have been used.^[8] A crucial aspect is the stabilization of the nanoparticles and the ability to rationally form either metallic, oxidic, semiconducting, and compound phases of the metal. There are very few reports of solid-state methods for preparing nanoparticles; the majority involve solution-based approaches, or colloidal chemistry.^[9] Aside from the standard approach to many nanoscale materials, more novel approaches have recently shown that Co_9O_8 and Ni_2P hollow nanocrystals can be prepared using the nanoscale Kirkendall effect.^[10,11] Organometallic complexes have also been used for metal-oxide nanostructure formation, by employing their sensitivity to moisture and the resulting exothermic decomposition.^[12]

Many of the routes that result in controllable and phase-pure metallic and metal-oxide nanoparticles are limited to metals and oxides due to the nature of the organometallic complex and its coordinative properties. Detailed observations of nanocrystallization during decomposition of solution-based organometallics are also relatively scarce. Obtaining single-crystal nanoparticles of any valve or transition metal as their

corresponding metallic and oxidic nanoparticles is a minimum next-step requirement; obtaining phosphate and, in addition, any other nanoscale compound by similar routes is a considerable advantage given the usefulness of nanoscale oxides and phosphates in lithium batteries for example. The method outlined here allows a simple and effective route to positive and negative thermal expansion materials as individual nanostructures or as a deposited film. Pyrophosphates $A^{IV}M_2^VO_7$, where the A^{IV} cation includes Zr, Ti, Mo, Re, W, Th, U, Pu, Ce, Hf, Pb, Sn, Ge, and Si; $M^V = P, V, \text{ or } As$, are known for their unusual high temperature behaviour.^[13] Thermal expansion is a necessary consideration in a number of applications where increases and decreases in temperatures can affect physical dimensions, stability, integrity, and mechanical properties of materials. To the best of our knowledge, there are no dedicated reports of controlled metal-phosphate nanomaterial synthesis through organometallic syntheses and subsequent procedures.

Chemical reactions of nanoparticles can also occur under exposure to the electron beam of a transmission electron microscope. Many of the previous reports on this phenomenon are linked to uncontrolled crystallization even though the information leads to a better understanding of the crystallization mechanism. Various mechanisms such as quasi-melting, particle diffusion and phase transition-resolidification have been reported for some time.^[14,15] Examples of nanocrystallization of anatase or rutile TiO_2 by laser treatment have been also reported^[15] and the transformation from core/shell $Se@C$ to yolk/shell $M/Se@C$ ($M = Au, Ag$) can be achieved through electron beam irradiation from the microscope.^[15] Controlling such reactions, allowed through electron beam induced heating interactions, is best achieved via organometallic routes, as is commonly observed in many applications such as focused ion beam metal deposition.

The molecular precursor route to nanostructured materials both in solution^[16-18] or in the solid-state^[19,20] is an unconventional, yet suitable, way to obtain metallic, metal-oxidic and semiconducting nanoparticles and nanostructures. Organometallic derivatives, both cyclic and polymeric phosphazenes, are emerging as useful precursors of metallic nanostructured materials.^[21-23] Precursors containing two different organometallic fragments coordinated to the phosphorus ring of a cyclotriphosphazene have not yet been successfully realized as nanomaterial precursors.^[24] This method is so versatile it allows us to form many

transition metals to form as oxide, phosphate and also pyrophosphates which offer high lithium-ion mobilities for fast charging lithium-ion phosphate-based cathode materials.^[25]

Here, we report the synthesis of new organometallic derivatives of cyclotriphosphazenes that result in individual single-crystal nanoparticles of metal oxides and phosphates embedded in an amorphous matrix after pyrolysis in air. Coordination of precursors (1) and (2) shown in Scheme 1 by Cp_2TiCl and $\text{W}(\text{CO})_5$ fragments is done to create new bi-organometallic derivatives (1a)-(2b) reported here. To our knowledge, these precursors are the first dinuclear heterobimetallic derivatives of cyclotriphosphazenes containing both silicon and a transition metal attached to the phosphazene ring.^[26] Pyrolysis at 800 °C in air result in nanostructured materials: using precursors (1a) and (2a) we produce both Ti and Si-containing single-crystal nanoparticles (TiO_2 and SiO_2) respectively, with the first report of Si and W-oxide and phosphate single-crystal nanoparticles from precursors (1b) and (2b). High resolution electron microscopy and various spectroscopic analyses were used to identify the elusive W and Si pyrophosphates (WP_2O_7 and SiP_2O_7) as either perfect single-crystal or heavily twinned nanoparticles formed using a solid-state method of direct deposition on a surface. We also detail the observation of single crystal nanoparticles of SiP_2O_7 formed *in situ* by electron beam-induced reaction of between the SiO_2 and remnant phosphazenes (post pyrolysis), and show the solid-state stabilizing effect of P_4O_7 formed from pyrolysis of their respective organometallic derivatives. This paper also details a mechanism for writing these nanoparticles into the host material using this pyrolytic approach at lower crystallization temperatures than bulk materials. One potential limitation with organometallic routes to nanomaterials is that they are almost all conducted in solution based form. This solid state method can replicate what is formed in solution based approaches, extends the technique to new nanomaterials through design of new phosphazene based polymeric precursors, but also allows for deposition on surfaces that do not wet, or are sensitive to, solution-based deposits.

2. Experimental Section

General: All reactions were carried out under nitrogen using standard Schlenk techniques. Infra-red (IR) spectra were recorded on an FT-IR Perkin-Elmer 2000 spectrophotometer. Solvents were dried and purified

using standard procedures. $\text{N}_3\text{P}_3\text{Cl}_6$, $\text{W}(\text{CO})_6$, $\text{H}_2\text{N}(\text{CH}_2)_3\text{Si}(\text{OEt})_3$, $\text{HN}(\text{CH}_3)(\text{CH}_2)_3\text{CN}$, $\text{HOC}_6\text{H}_4\text{CH}_2\text{CN}$, Cp_2TiCl_2 , and NH_4PF_6 (Sigma-Aldrich) were used as received.

Characterization methods: Nuclear magnetic resonance (NMR) spectra were conducted using a Bruker AC-300 instrument with CDCl_3 as the solvent unless otherwise stated. ^1H and $^{13}\text{C}\{^1\text{H}\}$ NMR are given in δ relative to TMS. $^{31}\text{P}\{^1\text{H}\}$ are given in δ relative to external 85% aqueous H_3PO_4 . Coupling constants are in Hz.

X-ray diffraction (XRD) was carried out at room temperature on a Siemens D-5000 diffractometer with θ - 2θ geometry. The XRD data was collected using Cu-K α radiation (40 kV and 30 mA). Scanning electron microscopy (SEM) and energy dispersive X-ray analysis (EDX) were acquired with a JEOL 5410 SEM with a NORAN Instrument micro-probe transmission microscope and with a Hitachi SU-70 FESEM operating at 10 kV equipped with an Oxford Instruments X-max 50 mm² solid-state EDX detector.

Transmission electron microscopy (TEM) was carried out on a JEOL JEM-2011 using a LaB₆ filament operating at 200 kV. The finely powdered samples were dispersed in *n*-hexane and iso-propyl alcohol (IPA), dropped on a conventional holey carbon copper grid and dried under a lamp. TEM image measurements and Fast Fourier Transform (FFT) analyses were made using DigitalMicrographTM software with a Gatan Multiscan 794 CCD camera.

The pyrolysis experiments were carried out by pouring a weighed portion (0.05 – 0.15 g) of the organometallic trimer into aluminium oxide boats placed in a tubular furnace (Lindberg/Blue Oven model STF55346C-1) under a flow of air, heated from 25 to 300 °C and then to 800 °C, and annealed for 2 h. The heating rate was 10 °C min⁻¹ under an air flow of 200 mL min⁻¹.

Synthesis of Precursors:

(1a) Synthesis of $\text{N}_3\text{P}_3[\text{NH}(\text{CH}_2)_3\text{Si}(\text{OEt})_3]_3[\text{NCH}_3(\text{CH}_2)_3\text{CN}\cdot\text{Cp}_2\text{TiCl}]_3[\text{PF}_6]_3$.

A mixture of $\text{N}_3\text{P}_3[\text{NH}(\text{CH}_2)_3\text{Si}(\text{OEt})_3]_3[\text{NCH}_3(\text{CH}_2)_3\text{CN}]_3$ (1.60 g, 1.534 mmol), and Cp_2TiCl_2 (1.14 g, 4.6 mmol) in the presence of NH_4PF_6 (1.12 g, 6.9 mmol) in methanol (60 mL) was stirred for 8 h at room temperature. The solvent was removed by decantation and the red solid formed was washed twice with a 1:1 *n*-hexane/diethyl ether mixture and dried under reduced pressure. Yield 2.2 g, 57%. Anal. for $\text{C}_{102}\text{H}_{123}\text{N}_{12}\text{O}_9\text{F}_{18}\text{Cl}_3\text{P}_6\text{Si}_3\text{Ti}_3$. Calc. (Found) C 52.41 (51.91), H 5.26 (5.84), N 7.9 (7.20%). ^{31}P NMR (CDCl_3) δ (ppm):

2.69, 1.25 (m, PN); -144.22 (PF₆). ¹H NMR (CDCl₃) δ (ppm): 1.20 (m, 36H, [(CH₂)₃Si(OCH₂CH₃)₃]); 0.58 (m, 27H, [(CH₂)₃Si(OCH₂CH₃)₃]); 6.51(m, C₅H₅). IR (KBr, cm⁻¹): 3419 (ν_{N-H}); 2941 (ν_{C-CH₃}); 2879 (ν_{C-CH₂}); 2362 (ν_{CN}); 1442 (δ_{Si-CH₂}); 1130, 1107 (ν_{PN}); 1016, 1012, 955 (ν_{Si-O}); 736, 720 (δ_{C-CH₃}).

(2a) Synthesis of N₃P₃[NH(CH₂)₃Si(OEt)₃]₃[OC₆H₄CH₂CN·Cp₂TiCl]₃[PF₆]₃.

A mixture of N₃P₃[NH(CH₂)₃Si(OEt)₃]₃[OC₆H₄CH₂CN]₃ (0.3063 g, 0.34 mmol) and Cp₂TiCl₂ (0.2577 g, 1.05 mmol) in the presence of NH₄PF₆ (0.2530 g, 1.55 mmol) in methanol (60 mL) was stirred for 8 h at room temperature. The resulting red solid was separated by decantation and washed twice with a 1:1 n-hexane/diethyl ether mixture and dried under reduced pressure. Yield 0.52 g 73%. Anal. for C₈₁H₁₁₄N₉O₁₂F₁₈Cl₃P₆Si₃Ti₃ Calc. (Found) C 40.97 (39.59), H 4.80 (4.52), N 5.3 (5.17%). ³¹P NMR (CDCl₃) δ (ppm): 3.2, 2.28 (m, PN); -144.11 (PF₆). ¹H NMR (CDCl₃) δ (ppm): 1.26 (m, 36H, [(CH₂)₃Si(OCH₂CH₃)₃]); 0.95 (m, 27H, [(CH₂)₃Si(OCH₂CH₃)₃]); 6.61 (m, C₅H₅). IR (KBr, cm⁻¹) 3314 (ν_{N-H}); 3111 (ν_{C-CH₃}); 2965, 2878 (ν_{C-CH₂}); 2361 (ν_{CN}); 1442 (δ_{Si-CH₂}); 1250 (ν_{PN}); 1047, 957 (ν_{Si-O}); 736, 720 (δ_{C-CH₃}).

(1b) Synthesis of N₃P₃[NH(CH₂)₃Si(OEt)₃]₃[NCH₃(CH₂)₃CN·W(CO)₅]₃.

N₃P₃[NH(CH₂)₃Si(OEt)₃]₃[NCH₃(CH₂)₃CN]₃ (0.5 g, 0.56 mmol) was added to W(CO)₅ generated photochemically by UV irradiation of W(CO)₆ (0.6 g, 0.1705 mmol), in MeOH (80 ml) at room temperature. The mixture was stirred for 20 h. The yellow solid formed was filtered off and washed with a 1:1 n-hexane/ether mixture twice and dried under vacuum. The solid was insoluble in the common solvents and then was characterized only by IR. IR (KBr, cm⁻¹): 3407 (ν_{N-H}); 2935 (ν_{C-CH₃}); 2886 (ν_{C-CH₂}); 2250 (ν_{CN}); 2075, 1981, 1925 (ν_{CO}); 1485 (δ_{Si-CH₂}); 1255, 1196 (ν_{PN}); 1100, 1047, 904 (ν_{Si-O}); 750, 695 (δ_{C-CH₃}). The low carbon content in the elemental analysis is due to the poor combustion of the sample.

(2b) Synthesis of (N₃P₃[NH(CH₂)₃Si(OEt)₃]₃[OC₆H₄CH₂CN·W(CO)₅]₃[PF₆]₃.

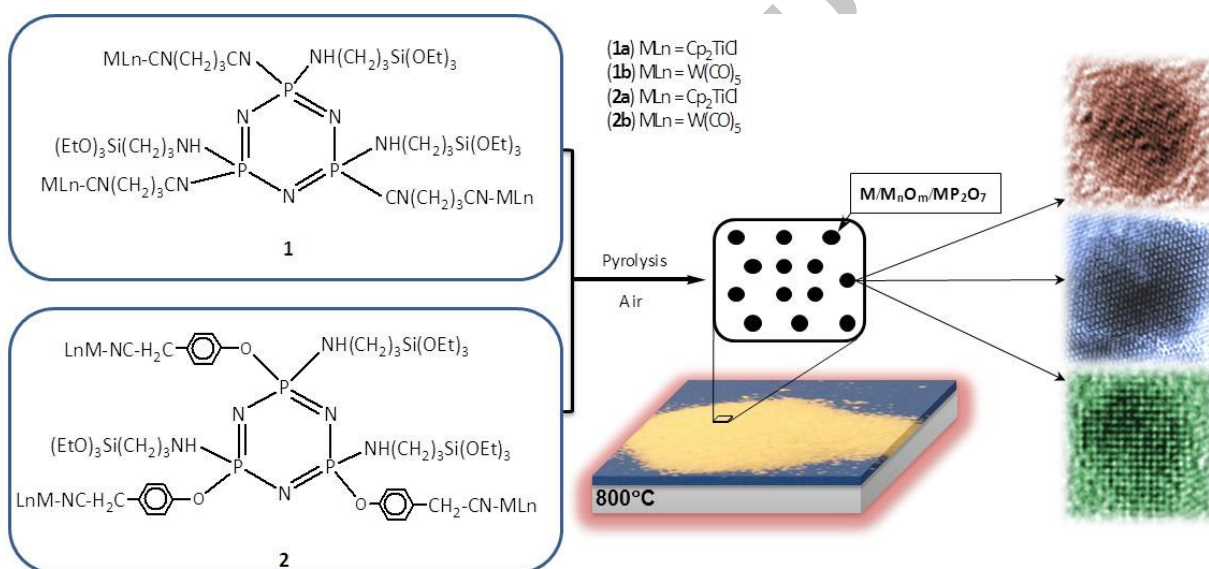
N₃P₃[NH(CH₂)₃Si(OEt)₃]₃[OC₆H₄CH₂CN]₃ (0.59 g, 0.568 mmol) was added to W(CO)₅ generated photochemically by UV irradiation of W(CO)₆ (0.6 g, 0.170 mmol), in MeOH (80 ml) at room temperature. The mixture was stirred for 20h. The yellow-brown solid formed was filtered off and washed with a 1:1 n-hexane/ether mixture twice and dried under vacuum. The solid was insoluble in the common solvents and then was characterized only by IR. IR (KBr, cm⁻¹) 3380 (ν_{N-H}); 2937 (ν_{C-CH₃}); 2879 (ν_{C-CH₂}); 2372 (ν_{CN});

2080, 1966, 1928 (ν_{CO}); 1443 $\delta(\text{Si-CH}_2)$; 1262, 1196 (ν_{PN}); 1099, 1049, 918 ($\nu_{\text{Si-O}}$); 760 ($\delta_{\text{C-CH}_3}$). Anal. for $\text{C}_{66}\text{H}_{84}\text{N}_{12}\text{O}_{27}\text{F}_{18}\text{Si}_3\text{W}_3$ Calc. (Found): C 35.65 (35.67), H 3.68 (3.7), N: 3.96 (4.07).

A detailed discussion of the analytical as well as spectroscopic data for precursors (1a), (1b), (2a) and (2b) is provided in Supporting Information S₁.

Synthesis of model precursors:

For comparison purposes, from the complex derivatives (1a), (1b), (2a) and (2b) shown in Scheme 1, we also prepared and characterized the model precursors $\text{HCH}_3(\text{CH}_2)_3\text{CN}\cdot\text{Cp}_2\text{TiCl}][\text{PF}_6]$ (4), $[\text{HOC}_6\text{H}_4\text{CH}_2\text{CN}\cdot\text{Cp}_2\text{TiCl}][\text{PF}_6]$ (5), $\text{HNCH}_3(\text{CH}_2)_3\text{CN}\cdot\text{W}(\text{CO})_5$ (6), and $\text{HOC}_6\text{H}_4\text{CH}_2\text{CN}\cdot\text{W}(\text{CO})_5$ (7). These are detailed in the Supporting Information.



Scheme 1. Formulas of the cyclotriphosphazenes containing Si and transition metal organometallic precursors. These precursors are placed on Si substrates in their solid state and pyrolyzed in air to form the nanoparticles.

3. Results and Discussion

3.1 Pyrolysis of the precursors and nanoparticle formation

Pyrolysis of $\text{N}_3\text{P}_3[\text{NH}(\text{CH}_2)_3\text{Si}(\text{OEt})_3]_3[\text{NCH}_3(\text{CH}_2)_3\text{CN}\cdot\text{CpTiCl}][\text{PF}_6]_3$ (1a) in air at 800 °C results in the formation of mainly tetragonal TiO_2 . This was also confirmed by XRD analysis, shown in Fig. 1a. The optical image in Fig. 1a shows the resulting material to be a fine white powder. The broad and relatively low intensity peaks in the double-angle 2θ range 10-28° can be assigned to P_4O_7 ^[21] and has been previously

observed in the pyrolysis of organometallic derivatives of polyphosphazenes^[22] and cyclotriphosphazenes.^[23,27] In addition, some relatively weak reflections are observed at $2\theta = 5.9^\circ$ and 6.4° suggest the formation of quantities of hexagonally ordered mesoporous SiO_2 .^[28] The SEM images exhibit a tridimensional porous network, as is shown in Fig. 1b, and also in the TEM image in Fig. 1d. EDX analyses (Fig. 1c) confirm the presence of mainly Si, Ti, P and O in agreement with the diffraction data and CHN analyses (see Experimental section).

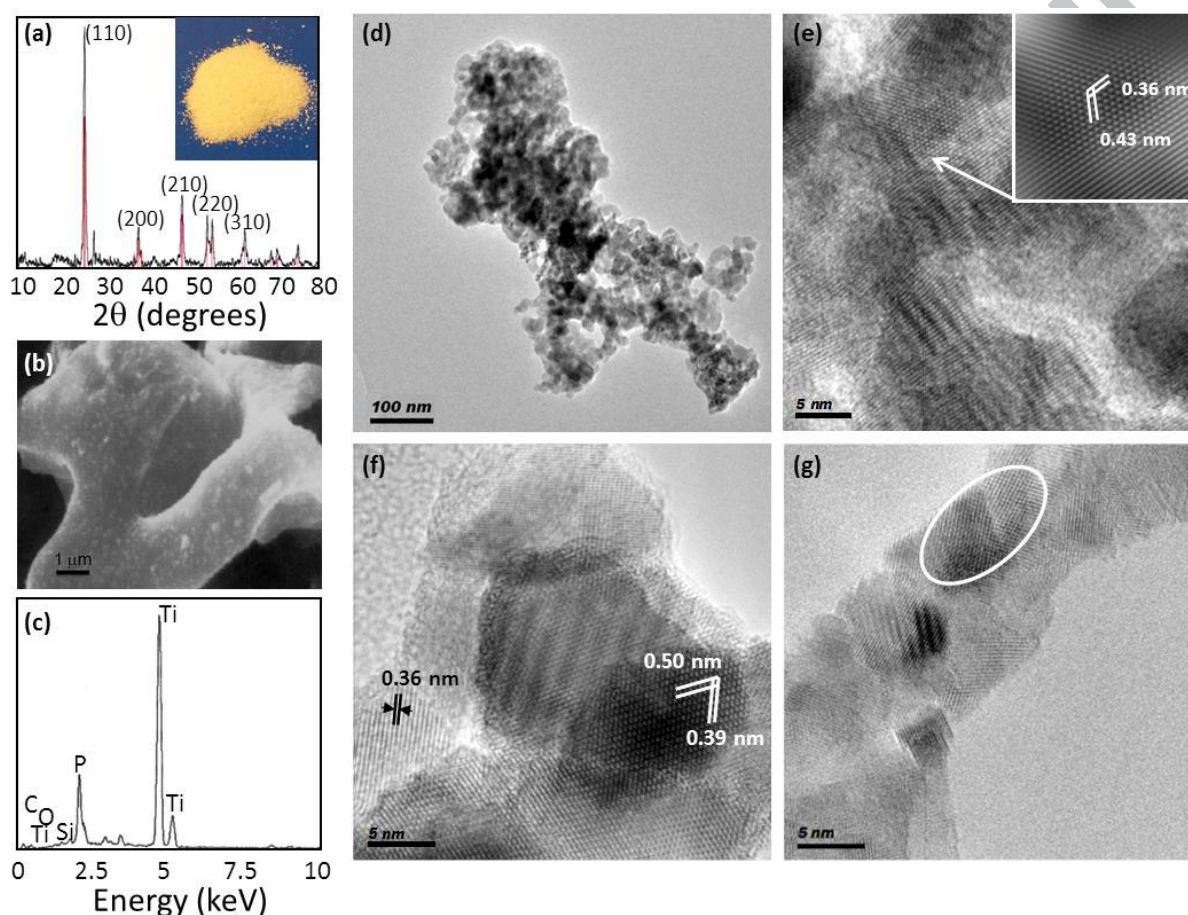


Figure 1. (a) XRD pattern with an optical micrograph of the product from (1a). The red vertical bars are the standard peaks of anatase TiO_2 . (b) SEM image and (c) EDAX profile of the pyrolytic product from (1a). (d) TEM image of the overall nanostructured product from precursor (1a). HRTEM images confirm the formation of (e) SiP_2O_7 (f) P_4O_7 and (g) TiO_2 nanocrystals embedded in an amorphous matrix. The inset to (e) is a filtered section showing the lattice fringe spacings.

The TEM analysis of the product is presented in Figs 1d-g. Figure 1d shows a low magnification survey image highlighting the porous network morphology. More detailed information was obtained by HRTEM where in Fig. 1e single crystal regions are observed with a measured fringe spacings of 0.36 nm and 0.43 nm which correspond to the separation between $\{200\}$ and $\{112\}$ planes of cubic SiP_2O_7 (Space

group: $Pa-3$). In addition, several regions containing single crystal nanostructures of monoclinic P_4O_7 (Space group: $P21/n$) are found and evidence is shown in Fig. 1f. Nanoparticles and crystals of P_4O_7 , suggested by previous work to exist and aid in the stabilization of the pyrolytic product during thermal decomposition, are observed for the first time. In Fig. 1f, the fringe spacing of the (020) planes of monoclinic P_4O_7 is 0.498 nm, corresponding to the observations (0.5 nm). We also identify the 0.39 nm lattice spacing of the (-211) planes of monoclinic P_4O_7 shown in the 2D HRTEM image of the nanocrystal. Finally, the major constituent of the product is that of TiO_2 , which typically forms as an aggregate of crystals. Larger regions of TiO_2 formation can be seen in Fig. 1g. Here, the highlighted region is of single crystals showing the (021) planes of orthorhombic TiO_2 (Space group: $Pbca$). IR spectra of the pyrolyzed product is very simple exhibiting broad bands at 1051 cm^{-1} , 603 cm^{-1} and 355 cm^{-1} which can be assigned to the $\nu(PO_4)^{[29]}$ and $\nu(Si-O-Si)$ vibrations^[30] (see Supporting Information, Fig. S1).

Pyrolysis of $N_3P_3[NH(CH_2)_3Si(OEt)_3]_3[OC_6H_4CH_2CN\cdot Cp_2TiCl]_3[PF_6]_3$ (2a) in air at $800\text{ }^\circ\text{C}$ also results in mainly anatase tetragonal TiO_2 ($I4/amd$)^[31] as was confirmed by XRD (see Supporting Information, Fig. S2a). Unlike (1a), this material forms as a dry foam comprising two distinct regions as shown in the optical image in Fig. 2a: the first is a black product, the second is white, both of which form during pyrolysis. Similar to the pyrolytic product from (1a), the broad, weak intensity reflections at $\sim 2\theta = 20^\circ$ are indexed to P_4O_7 where the low intensity reflections between $2\theta = 1-10^\circ$ indicate some presence of mesoporous hexagonal SiO_2 , similar to (1a). The SEM image in Fig. S2b shows the pyrolytic product exhibits a porous cauliflower-like morphology consistent with dry foam with corresponding EDX analyses confirming that this material contains mainly Ti, Si, P and O in agreement with diffraction data.

The HRTEM analysis of the pyrolytic product from (2a) in Figs 2a,b shows two distinct product types resulting from pyrolysis: the first (Fig. 2a) contains pure inorganic material, the second (Fig. 2b) being predominantly inorganic interspersed in an organic matrix. A characteristic feature of the second case is the formation of discrete nanocrystals within the amorphous host matrix. The two regions can be classified in terms of their crystallinity; the material in Fig. 2a being of higher crystallinity throughout. HRTEM investigations of the products confirm the dominant presence of nanostructured tetragonal TiO_2 in agreement with XRD and EDX measurements. HRTEM also confirmed the presence of orthorhombic

SiO₂ in crystalline form in a few regions of the sample, but not as individual nanoparticles (see Supporting Information, Fig. S3). All resulting crystals have similar morphology and from Figs 2a and c, we observe localized variation in crystal thickness, shown more clearly in the variable focus HRTEM images in Supporting Information, Fig. S4. This observation is most probably due to incomplete crystallization of the pyrolyzed organometallic derivative. We did not observe quasi-melting or heating decomposition by the electron beam, as this would result in the brighter regions in Figs 2a,c and Fig. S4 being decomposed voids rather than crystalline materials of just locally reduced thickness. High resolution imaging in Fig. 2c of the crystal marked with an arrow in Fig. 2a, shows a 2D single crystal with a measured lattice spacing of 0.32 nm which corresponds to d-spacing between (110) planes of tetragonal TiO₂. Apart from the particle containing region in Fig. 2b, the rest of the material is crystalline, forming a mesoporous network.

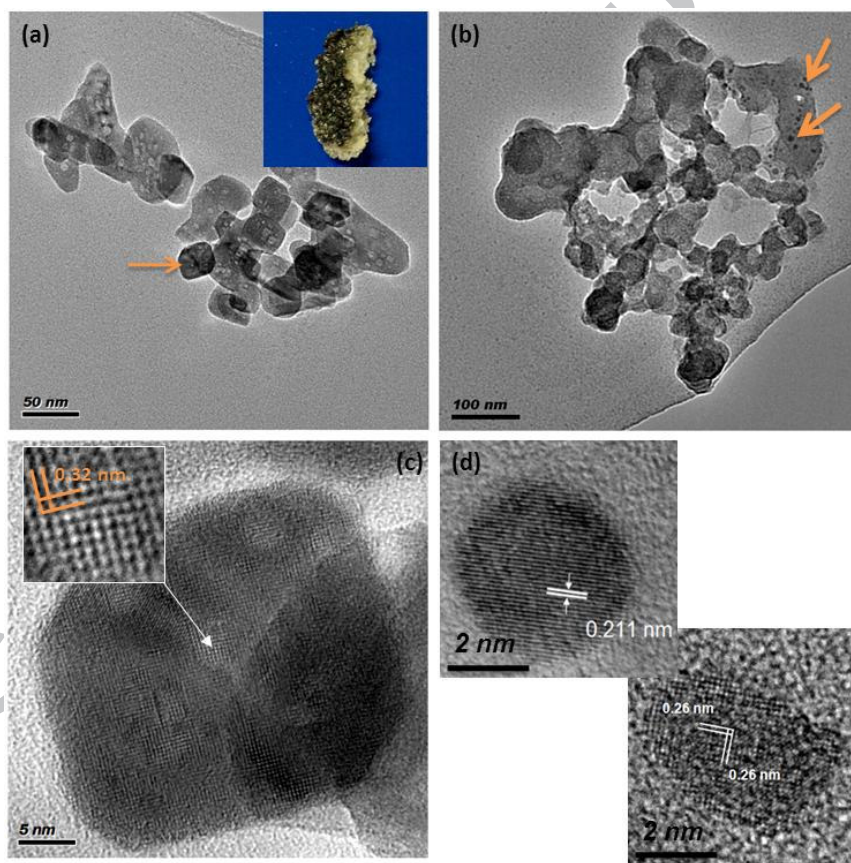


Figure 2 (a) TEM image of the overall nanostructured product showing the segregated formation of single-crystal TiO₂ and (b) TiO₂ and SiP₂O₇ nanocrystals. (c) HRTEM image of a single TiO₂ nanocrystal highlighted by an arrow in (a), and (d) TiO₂ and SiP₂O₇ single-crystal nanoparticles.

HRTEM investigation of the nanoparticles in Fig. 2b confirms the presence of individual single crystal embedded nanoparticles with diameters of ~5 nm. Analysis of electron diffraction data and lattice

fringe spacing from particles found in this material (see Fig. 2d), indicates that these nanoparticles are SiP_2O_7 where the lattice spacing of 0.211 nm corresponds to the d-spacing between (221) planes of TiO_2 , and 0.25 nm indicative of the lattice spacing between (220) planes of cubic SiP_2O_7 ($Pa-3$). Thus, the black powder is represented at high magnification in Fig. 2a with the white represented by Fig. 2b. It is clear from XRD and HRTEM that the white powder is composed of crystalline material consisting of SiP_2O_7 (with some evidence for spherical TiO_2 nanoparticles), while the black powder comprises TiO_2 nanocrystals only. Corresponding IR spectra of the pyrolyzed product gives a very simple spectrum exhibiting broad bands at 1064 cm^{-1} , 619 cm^{-1} and 350 cm^{-1} , which is similar, as expected, to that from the pyrolytic product from model precursor (4) (see Supporting Information, Fig. S5). These vibronic absorptions are well known and can be assigned to the $\nu(\text{PO}_4)$ and $\nu(\text{Si-O-Si})$ stretching vibrations.

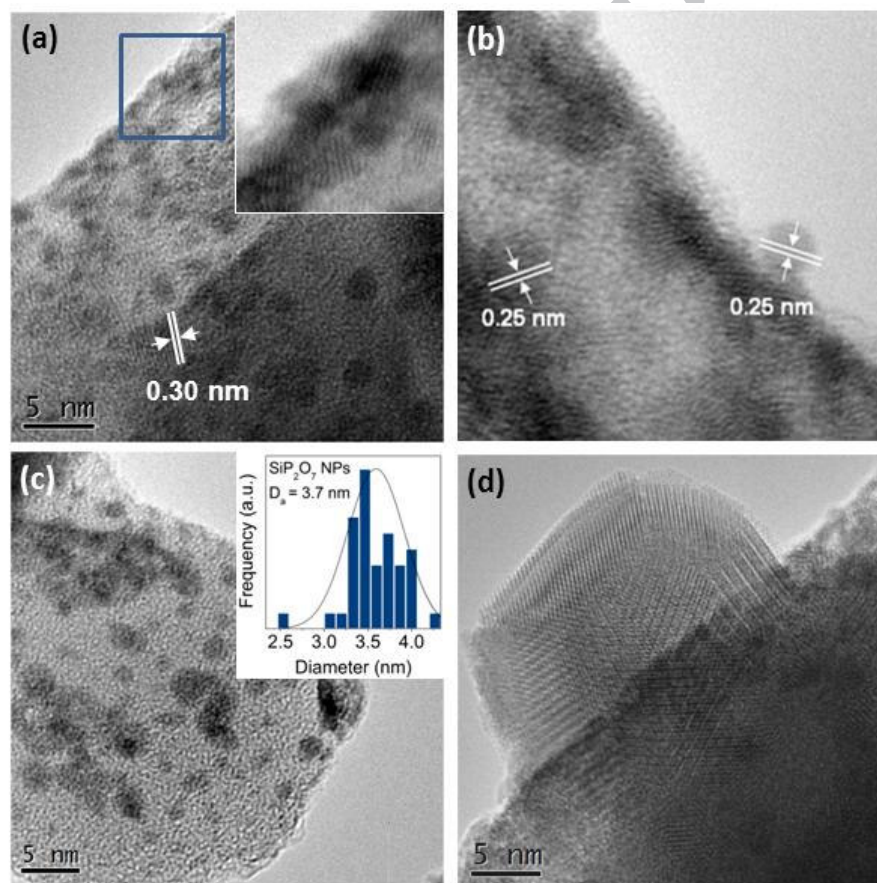


Figure 3 (a-c) TEM images of the overall nanostructured product from (1b) showing embedded single-crystal SiP_2O_7 nanoparticles. (*Inset*) Histogram of measured SiP_2O_7 nanoparticle diameters derived from multiple TEM images. (d) HRTEM image of a larger 3D tetragonal SiP_2O_7 crystal with a high density of twinning and stacking faults.

Pyrolysis of trimer precursor (1b) containing W and Si results in a somewhat complex mixture mainly comprising phases of SiO_2 , SiP_2O_7 , WO_3 and P_4O_7 . The resultant product is a black, pumice-like clumped powder as shown in the SEM and optical micrographs in Supporting Information, Fig. S6. A complex XRD pattern was observed where the presence of these phases was identified (see Supporting Information, Fig. S7). HRTEM investigations of the product from pyrolysis of this precursor (1b) show that the resulting product is characterized by an amorphous organic phase embedded with single crystal nanoparticles. Figure 3a shows HRTEM images of a cluster of nanoparticles. Resolved lattice fringes show the interplanar spacing measured to be 0.3 nm, between the (211) planes of cubic SiP_2O_7 . Figure 3b shows single-crystal particles where the lattice spacing is measured as 0.25 nm corresponding to the (220) interplanar spacing of SiP_2O_7 . Overall, this precursor affords the highest density of embedded nanoparticles in the pyrolytic product of all precursors investigated; Fig. 3c shows an example of a high density nanoparticle-containing region. Measurements of nanoparticles diameters from HRTEM images indicate the predominant formation of nanoparticles with diameters in the range 2-5 nm, with an average diameter of 3.7 nm. In some areas, large heavily defective nanoparticles were observed (Fig. 3d) which is indexed to tetragonal SiP_2O_7 . Corresponding EDX analysis confirmed the presence of Si, W, P and O.

Lastly, we present the pyrolytic nanostructured product from precursor (2b). The SEM image in Fig. S8 shows that the product is a porous powder with EDX showing the presence of Si, P, C, O and W. Again, XRD patterns for the product from pyrolysis of (2b) identify phases of SiO_2 , SiP_2O_7 , WO_3 , WP_2O_7 and P_4O_7 (see Supporting Information, Fig. S9). HRTEM investigations show two distinct regions: one containing crystalline platelet-like particles (Fig. 4a) and the second being an amorphous matrix in which large single crystalline material and nanoparticles are embedded. Figure 4b shows a typical arrangement of the pyrolytic product. The material is a mesh-like arrangement of interwoven polycrystalline materials containing the nanoparticles. C-H-N elemental analysis and EDX measurements showed that this precursor contains a much larger carbon content (see Experimental section) as is expected from the synthetic route. HRTEM and electron diffraction analysis shows the structures are single crystal entities, as shown in Figs 4c,e, and are identified as WP_2O_7 . The 0.39 nm lattice spacing corresponds to the (002) interplanar spacing of cubic WP_2O_7 (Space group: $Pa-3$). The HRTEM analysis of the amorphous regions of the pyrolytic product from

precursor (2b), shown in Fig. 4b, shows the presence of single crystal nanoparticles identified as WP_2O_7 throughout the amorphous matrix as seen in Fig. 4d. Analysis of embedded nanoparticle diameters from TEM images, an example of which can be seen in Fig. 4f, gives a distribution over the range 3-7 nm, with an average nanoparticle diameter of 5.3 nm.

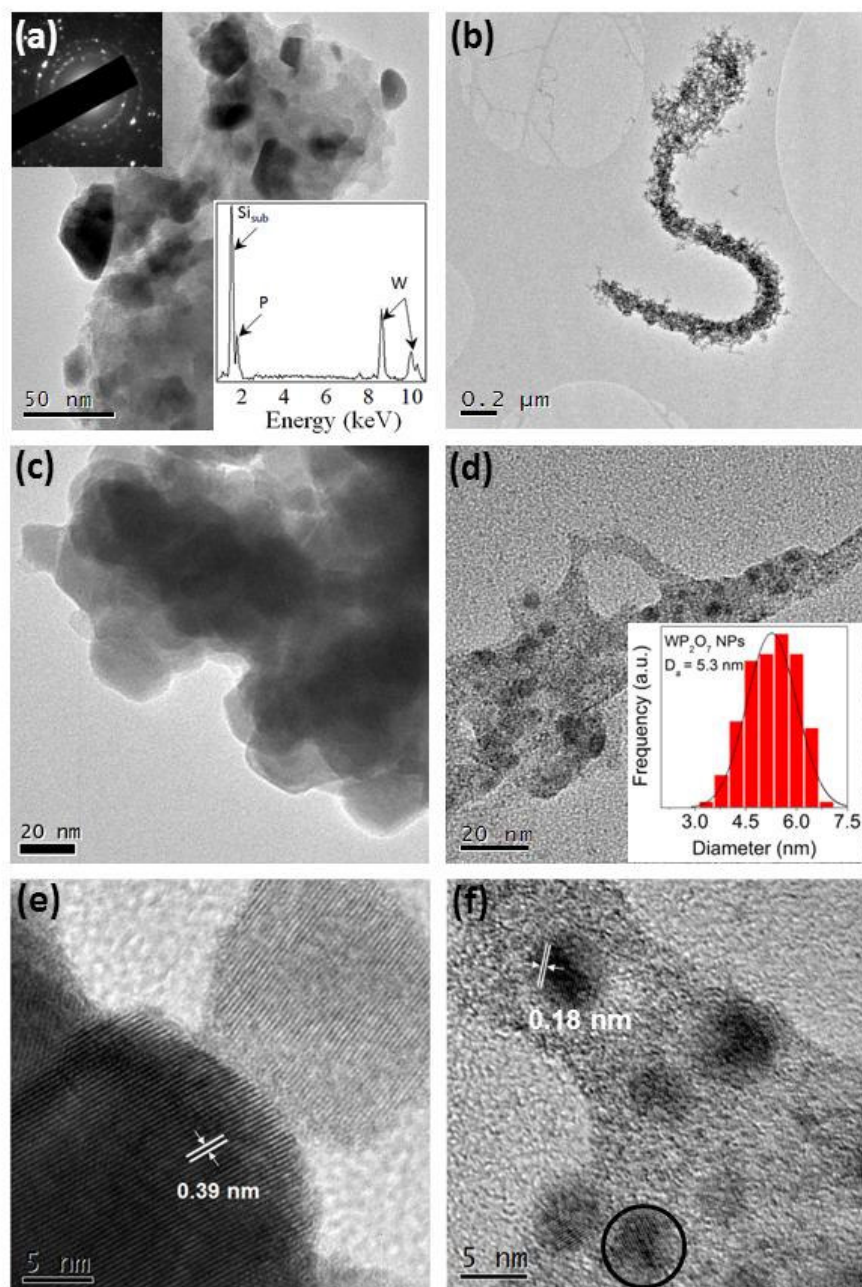


Figure 4(a) TEM images of the overall product from (2b) showing large crystals in an amorphous matrix. The inset show the electron diffraction pattern of the overall product and the EDX profile of the material. (b) TEM image of the overall nanostructured product. (c,d) HRTEM images from (a) and (c), respectively, showing single-crystal WP_2O_7 nanoparticles. The inset shows a histogram of particle diameter variation. (e) HRTEM image of the larger crystals from (a). (f) HRTEM image of a region showing several single crystal WP_2O_7 nanoparticles.

3.2 Structural Characterisation of Phosphate Nanoparticles

The WP_2O_7 structure has only recently been resolved and this route results in the first nanoparticles of this crystal.^[32] HRTEM images of the single crystal WP_2O_7 nanoparticles are presented in Figs 5a,b and show the cubic order of the nanoparticle and lattice fringe spacings corresponding to the (111) interplanar distance of cubic WP_2O_7 .

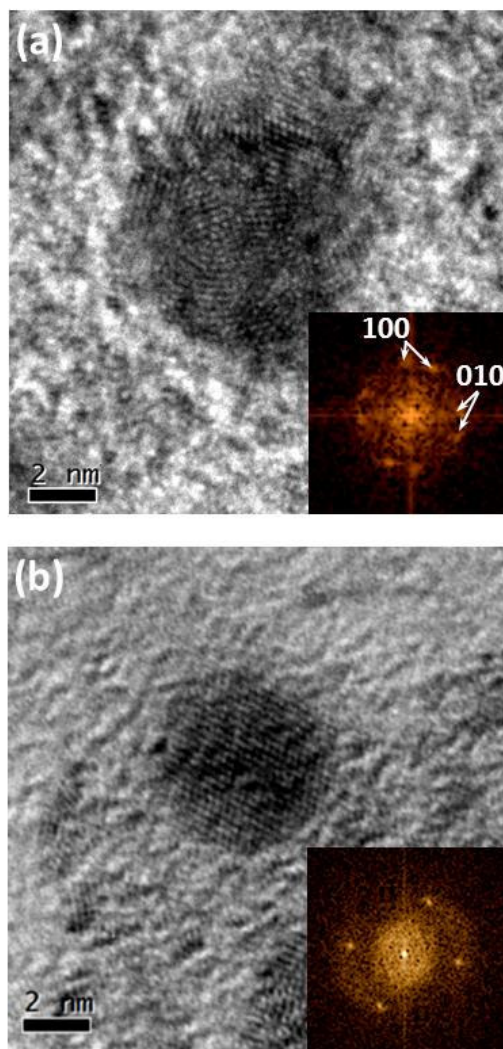


Figure 5 HRTEM images of individual single crystal WP_2O_7 nanoparticles. (a) A heavily faulted nanoparticle showing multiple twin boundaries. The associated FFT (inset) shows 8 spots with twinned pseudocubic symmetry. (b) HRTEM image of a WP_2O_7 nanoparticle exhibiting perfect crystalline order, evidenced by its 2D FFT pattern.

The corresponding FFT patterns for Figs 5a and b show that cubic WP_2O_7 nanoparticles can form as heavily twinned nanocrystals or as perfect single crystal nanoparticles. Here, the twins are defects that results in mirrored crystal planes about a twin axis within the crystal structure. This has been previously

observed during sintering of SiO_2 nanoparticles.^[33] The FFT for Fig. 5a clearly exhibits 8 spots with twinned pseudocubic symmetry. The (100) and (010) spots from the cubic FFT rotated by 30° . In Fig. 5b, the four spots expected from cubic/tetragonal symmetry are observed. Figure 6 also shows twinned WP_2O_7 nanoparticles, which are the most common growth defects observed. In Fig. 6a, the HRTEM image shows a single particle where we observe $\{111\}$ twins. Analysis of corresponding FFT patterns taken from each side of the crystal shows that the $\{111\}$ planes are mirrored. The measured angle between the $\{111\}$ planes across the boundary in Fig. 6 is $\sim 70^\circ$. This agrees with the observation that the (111) spot in the corresponding FFT rotates by $\sim 35^\circ$.

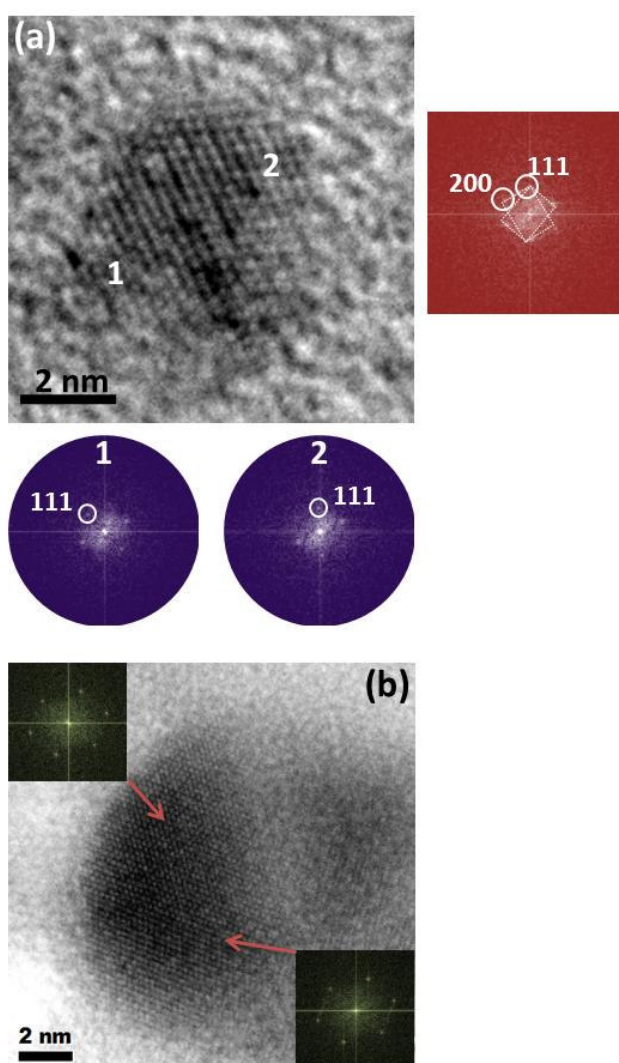


Figure 6 (a) HRTEM image of an individual single crystal WP_2O_7 nanoparticles exhibiting a single coherent twin defect. The FFT patterns underneath are derived from regions 1 and 2 from the TEM image. The FFT on the right is from the entire particle showing the twin boundary to be along the (200) plane with the $\{111\}$ planes at an angle of 35.2° to either side of the boundary. (b) Nanotwin in WP_2O_7 nanoparticle in the $[011]$ zone axis. The nanotwin has a non coherent boundary, which produces streaks in the power spectrum.

Figure 6b also shows a similarly twinned nanoparticle of WP_2O_7 acquired from a separate analytical sample. Again, a similar twin defect is observed as evidenced by streaking in the FFT. The nanoparticles are never observed to agglomerate or sinter and are predominantly found as individual particles throughout the amorphous regions. EDX analysis of the amorphous region shows it contains W, P, Si, and O and is most probably a mixed phase of WO_3 and/or amorphous SiO_2 . This last precursor is of considerable interest since WO_3 and WP_2O_7 can be formed.

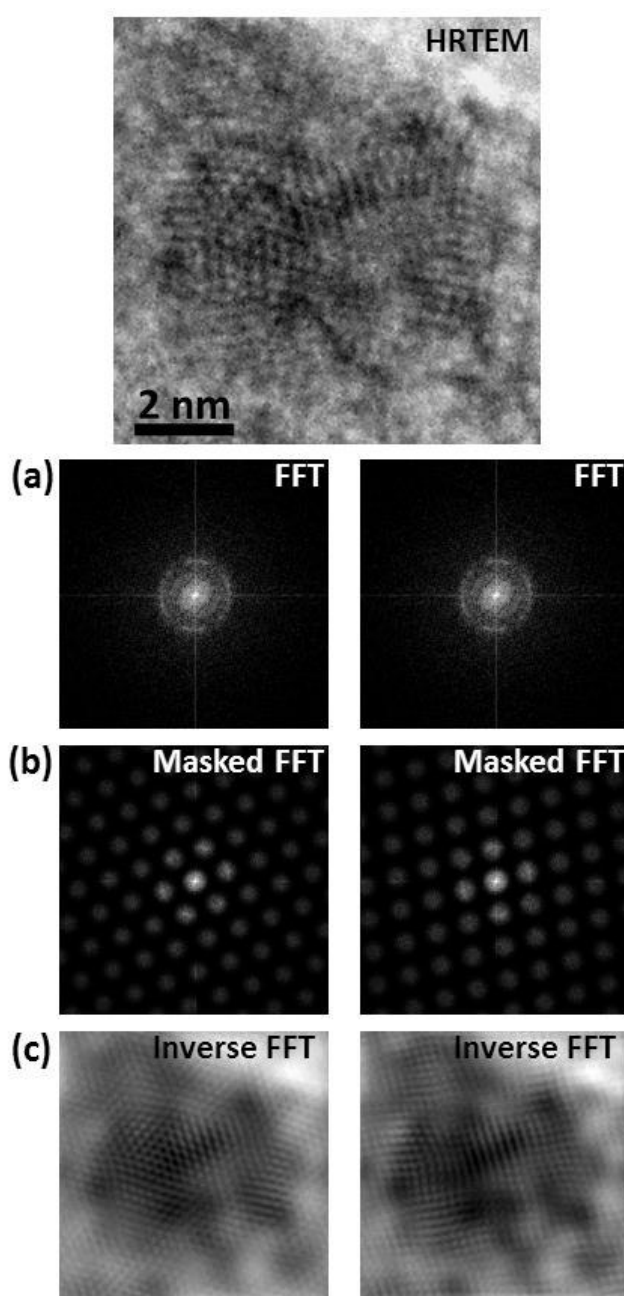


Figure 7 HRTEM image of three-fold twin boundaries in a cubic WP_2O_7 nanoparticle. The corresponding FFT analysis comprises (a) the direct FFT, (b) masked FFT patterns of 3-fold (left) and 2-fold (right) symmetry reflections and (c) corresponding inverse FFT images.

Assessing the symmetry of twinned and faulted structures was done by comparing 2- and 3-fold symmetry in the power spectrum (FFT) of the TEM images. In Fig. 7, a WP_2O_7 nanoparticle is shown, and similar to Fig. 5, exhibits multiple twinning. The HRTEM image in Fig. 7a was reconstructed from its Fourier transform, limiting the reconstruction to 2 and 3-fold symmetry. It is clear that the original image is dominated by a 3-fold twin boundary, whereas 2-fold symmetry in the lattice results in an inaccurate reconstruction of the original image. Twinned and heavily faulted structures are the most commonly observed for WP_2O_7 here and the thermal treatment results in fully crystallized nanoparticles characterized by a high density of twin boundaries of various order. No considerable change in particle size is noted and no amorphous shell is found on any of the embedded particles examined.

3.3 *In situ* electron beam-induced nanoparticle formation

In contrast to the W-containing phosphate nanoparticles, we observe that the SiP_2O_7 (from precursor 1b) can also be formed *in situ* by heating interaction from the electron beam at 200 kV, between the by-products of the pyrolysis, SiO_2 , phosphazenes and P_4O_7 . *In situ* formation of SiP_2O_7 happens in the presence of SiO_2 and unreacted phosphazenic components, stabilized by P_4O_7 , and is discussed in terms of organometallic decomposition to the pyrophosphate phase. Solid-state reaction of SiO_2 with phosphorus oxides gives rise to SiP_2O_7 ^[34-36] at the macroscale. Previous routes to the synthesis of metal phosphates, using SiP_2O_7 as a reagent, showed that the reaction of SiP_2O_7 with metal oxides yields a solid mixture of silica and metal phosphates; its reaction with metal fluorides yields solid metal phosphates and gaseous mixtures of SiF_4 and POF_3 .

Nanometer scale precision in nanoparticle formation through localized electron beam-induced reaction of the SiO_2 and remnant phosphazene in a P_4O_7 amorphous product from pyrolysis of (1b) is shown in Fig. 8. In Fig. 8, two regions (Fig. 8a,b and Fig. 8c-e) consisting of amorphous SiO_2 , unreacted phosphazene and P_4O_7 are examined. These regions are the predominately amorphous areas of the overall pyrolytic product shown in Fig. 3a. The crystalline-amorphous contrast of this region is seen more clearly in Supporting Information, Fig. S3, where large regions of crystalline SiO_2 are observed. In Fig. 8a we observe a SiP_2O_7 single crystal. In Fig. 8b this crystal is accompanied by another, exhibiting the same orientation at the first

where the 0.36 nm spacing between (220) planes of cubic SiP_2O_7 are found. In a close-by region, prolonged imaging results in significant crystallization of the already pyrolyzed product. In Fig. 8, common regions between pairs of images (a,b and c,d) are shown by arrows. The inset FFT of each of these regions are also shown where it is observed that spots with a distance of 0.386 nm^{-1} from the centre increase in number and intensity with continued exposure to the electron beam. All spots correspond to the (220) planes of the cubic SiP_2O_7 , and new spots correspond to the formation of new crystalline regions with different spatial orientations in the plane. It is clear that continued crystallization of self-similar nanoparticles and nanocrystals occurs with continued beam exposure.

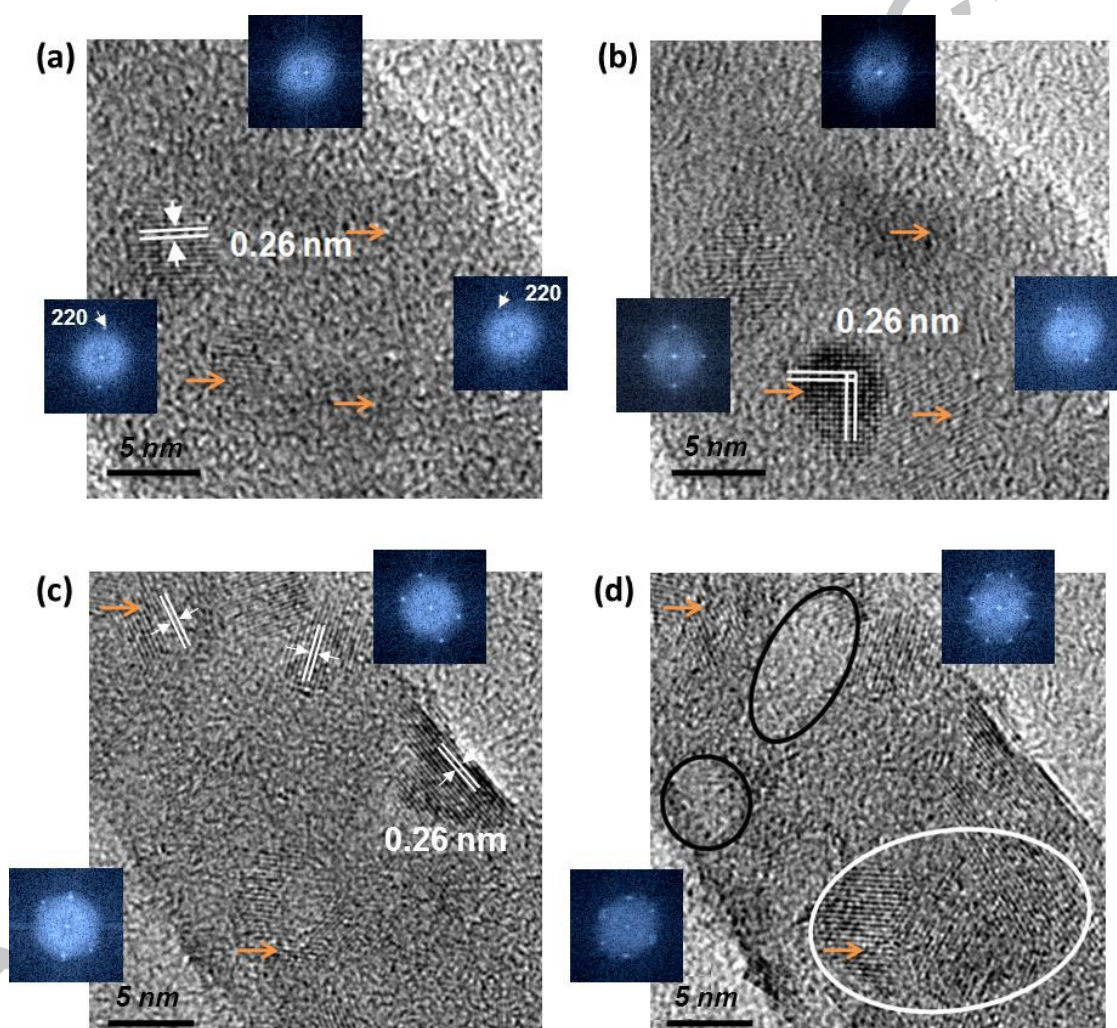


Figure 8 In situ HRTEM images of the reaction between amorphous SiO_2 and P_4O_7 to give crystalline SiP_2O_7 . Two separate regions are shown: Region 1 consisting of (a) and (b), and Region 2, consisting of (c) and (d). Common areas in the structure are highlighted by arrows and regions of interest are circled. These regions are also shown by their FFT patterns in each image.

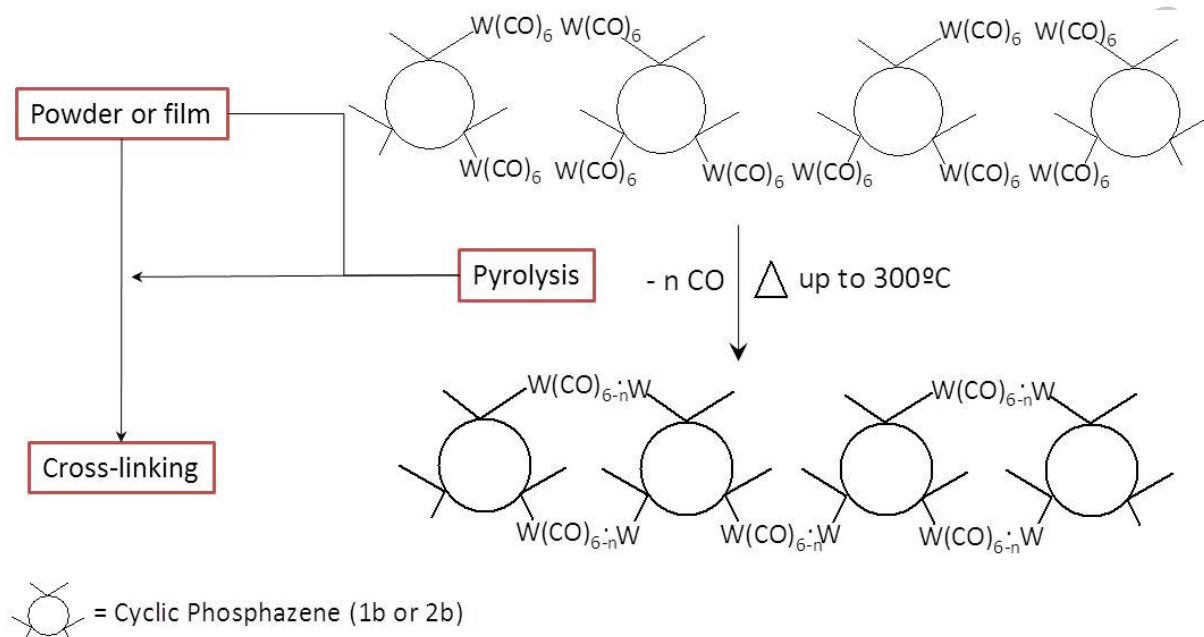
Figure 8c shows a region that was originally completely amorphous. Electron beam exposure results in the formation of two obvious SiP_2O_7 nanoparticles with significant crystallization as coalesced regions forming (Fig. 8d). In Fig. 8d, we note that voids are formed next regions where crystallization occurs indicating the consumption of the amorphous matrix in forming the crystalline material. The amorphous recrystallization causes densification of the material similar to sintering. All individual nanoparticles form single-crystals with the same respective orientation to the beam; for the (220) planes of cubic SiP_2O_7 , the beam-induced reaction forms particles with their (220) planes. This mainly happens for *in situ* formed nanocrystals; we note that cubic SiP_2O_7 particles formed during initial pyrolysis are rotated and sometimes also result in heavily twinned crystal structures. Thus, the approach allows ordered crystal growth with the possibility of forming pyrophosphate surfaces and full phases, depending on the exposure to the ebeam, which gives an alternative to substoichiometric tuning of the phosphate to form pyrophosphates.^[25]

3.4 Amorphous recrystallization of SiP_2O_7 and WP_2O_7 nanoparticles

The data presented shows that individual nanoparticles can be formed both during the pyrolysis of the precursors and also be electron-beam induced reaction of these products to form different nanoparticle phases. In all cases, particles rather than core-shell structures are formed indicating a true phase conversion reaction to form a new single crystal phase. During pyrolysis of bimetallic iron and thallium derivatives of polyphosphazenes,^[37] core-shell structures were observed and it was reported that this morphology was due to the regular distribution of the Fe and Tl centers along the polymeric chain, which is not the case for the cyclic trimer precursors (1a) – (2b) reported here. The initial release of the Si groups could give rise to the respective SiP_2O_7 nanoparticles separately from WO_3 , TiO_2 or SiO_2 , whose formation occurs after this initial step.^[22]

The formation in air of the nanostructures from the organometallic cyclic phosphazenes can be summarized by the loss or decomposition of some ligands of the organometallic fragment to produce vacant sites, producing a cyclomatrix network.^[23] Scheme 2 represents the initial thermal decomposition, where it has been shown^[34] that the organometallic fragments $\text{Mo}(\text{CO})_5$ and $\text{Mo}(\text{CO})_4\text{py}$ linked to the phosphazene precursors, respectively, lose carbon monoxide through decarbonylation upon heating to 300 °C. Extensive

cross-linking leads to W centers that migrate toward the vacancies generated in the cyclomatrix. Similarly, the phosphazenic phosphorus and the nitrogen polymeric chain evolve as the respective oxides upon oxidation, and do so as single crystals. The efficiency in decomposition is much higher in W-containing precursor compared to Si-containing precursors, which explains the remnant presence of phosphazenic components in Si after pyrolysis.



Scheme 2 Schematic representation of early stage decarbonylation of cyclotriphosphazenes containing W organometallic precursors (<300 °C). The circular moieties represent the N_3P_3 phosphazene rings. Each of the 6 lines emerging from the N_3P_3 phosphazene rings represent the $P-NH(CH_2)_3Si(OEt)_3$, $P-OC_6H_4-CH_2CN$ or $P-NCH_3(CH_2)_3CN$ branches. This scheme hold for precursors 1b and 2b, *i.e.* with $ML_n = W(CO)_5$.

Subsequent calcination of the organic matter produces holes in this cyclomatrix network, causing the agglomeration of the metallic particles, while oxidation of the phosphorus chain forms phosphorus oxides which bond to the metals to give metal phosphates and/or phosphorus oxides, and act as a solid-state matrix stabilizing the metal-oxide and metal-phosphate nanoparticles. Shi showed^[38] that nanoparticles in a matrix exhibit different melting temperatures: lower than the corresponding bulk melting temperatures in an oxide host, higher in a carbon host. The efficient decarbonylation step ensures the product is not embedded in a C-containing host. For the WP_2O_7 and SiP_2O_7 , their bulk melting temperatures are $T_{m,WP_2O_7} = 1100$ °C and $T_{m,SiP_2O_7} = 1250$ °C and so their crystallization at 800 °C agrees with an oxide host influence. As will be outlined below, P_4O_7 does indeed stabilize both SiP_2O_7 and WP_2O_7 crystallization, but since the pyrolysis efficiency of the W-containing precursor is higher and WP_2O_7 exhibits negative thermal expansion, only

SiP₂O₇ can be further formed in-situ after pyrolysis. Since (2b) contain carbon rings and was determined to have a greater C content (see Experimental section), the presence of excess carbon after pyrolysis would raise the melting temperature for decomposition. It is from (2b) that WP₂O₇ nanoparticles are chiefly found, with SiP₂O₇ in (1b). It must be remembered that individual nanoparticles of WP₂O₇ and SiP₂O₇ are already formed during pyrolysis and stabilized by the P₄O₇; for electron beam induced recrystallization to SiP₂O₇, it is believed that unreacted phosphazenic components after pyrolysis allowed continued crystallization to SiP₂O₇ by consumption of the amorphous SiO₂ in the matrix. The reason a pyrolysis temperature of 800 °C was chosen, was to ensure optimum decarbonylation processes at 300 °C quickly and efficiently so as to allow the host amorphous phase to form with subsequent localized crystallization of the metal centers to occur. At 800 °C, the recrystallization process in an oxidic host occurs at a lower temperature that is normally required for many oxide phases (often > 1000 °C), for example. Due to the interfacial thermal conductivity between guest particles and host material, phase sublimation is not observed.

Electron beam-induced nanoparticle formation results from the reaction between the by-products of pyrolysis. For this reaction to occur, significant heating must be caused by the electron beam interactions. The electron beam (intensity of $\sim 3 \times 10^{20} \text{ e cm}^{-2} \text{ s}^{-1}$) hits a dense amorphous mixture of SiO₂ and unreacted phosphazenes in the presence of P₄O₇ allowing them to react to form SiP₂O₇. Random events generating considerable phonon scattering may give rise to sufficient localized Joule heating. This constitutes an upper temperature limit that is less than the bulk melting temperature of SiP₂O₇ and also WP₂O₇. This triggers a melting or phase-transition-recrystallization process.

Crystallization is also found for WP₂O₇ nanoparticles, but the resulting nanostructures remain as particles and do not sinter or progressively crystallize/coalesce as is the case for SiP₂O₇. Figure 9 shows a HRTEM image of a region of the pyrolytic product (2b) selected to show the stages in WP₂O₇ crystallization within the host during pyrolysis. The image reveals 1.5 – 2 nm clusters with medium range annular contrast features (boxed region). This observation is reminiscent of Si nanoparticle sintering from amorphous powders^[39] where a nucleus acts as a crystallization seed point in the amorphous host matrix, resulting in crystalline regions being formed in time. A separate region of the pyrolytic product from (2b) also shows that amorphous crystallization occurs, without the consumption of the surrounding amorphous host. Figure

9b shows a series of HRTEM images and their corresponding FFT patterns. Some degree of crystallization does occur during electron-beam irradiation as noted by increased ordering in the FFT and in the lattice resolution in the HRTEM images. These clusters are believed to be the building blocks of the nanoparticles, and electron beam induced formation effectively ‘writes’ them into the host material. Stable crystallites nucleate around these localized ordered regions and growth proceeds by atomic rearrangement at the amorphous-crystalline interface. The transformation from an amorphous to crystalline state may be regarded as a decomposition of the amorphous phase SiO_2 or WO_3 to the nanosized crystallites in a P_4O_7 amorphous host which is partially consumed, as detailed schematically in Fig. 9c. Previous analysis using Gibbs free energy considerations for Si nanoparticles in an oxide host agree with the present results where the crystalline phase is stabilized by the amorphous host.^[40]

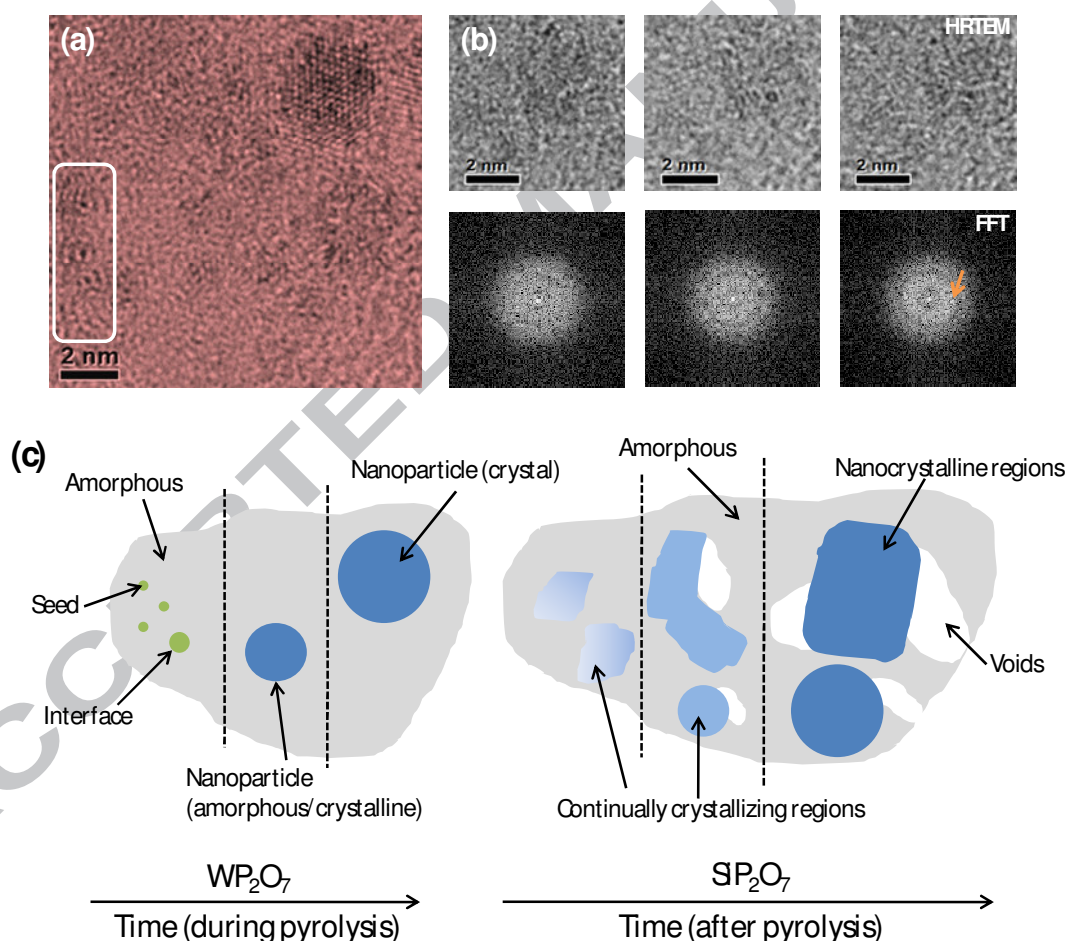


Figure 9 (a) HRTEM image of a single-crystal WP_2O_7 nanoparticle formed during pyrolysis. The boxed region highlights 1.5 – 2 nm clusters with medium-range order. (b) *In situ* HRTEM images of the crystallization WP_2O_7 . The corresponding FFT show the increase in crystal order with time. (c) Schematic representation of WP_2O_7 crystallization and also of *in situ* sintering crystallization of SiP_2O_7 .

3.5 In-situ crystallization model for embedded seed and crystal growth

The crystallization during pyrolysis and also the secondary crystallization (of 1b) by e-beam interactions can be analyzed using geometrical analysis of crystallization volume fractions within an amorphous oxide matrix. Figure 10 shows a schematic outline of a section of the material modelling the crystalline, amorphous and interfacial regions. The analysis considers the seeding and crystallization of spherical particles in an oxide host (which also stabilizes the resulting crystal formation) and involves amorphous recrystallization and consumption (in the case of precursor (1b)) of some of the host material containing remnant phosphazenic components. The model is valid for carbon-containing hosts also, so long as the higher melting temperatures are accounted for during crystallization. Using crystallization kinetics developed by Gutzow *et al.*^[41] for sintering processes, we describe below a geometrical consideration for nanoparticle crystallization during pyrolysis and e-beam interaction, *i.e.* under thermal excitation. As seen in Figs 9a and b, initial crystalline seeds form. Based on TEM imaging, we estimate a density of seeds, S_D to be $\sim 0.014 \text{ nm}^{-2}$. This translates to $70/4\pi R_R^2$ based on the model schematic in Fig. 10, where $R_R = 20 \text{ nm}$. R_R is the radius of the region of interest (assumed spherical in the analysis) composed of the reactants and the host material of P_4O_7 and less than fully carbonized phosphazenes. The radius r_C of the seed particles as determined from HRTEM, and R_C is the final radius of a nanoparticle up to the point of contact with another nanoparticle or crystalline region.

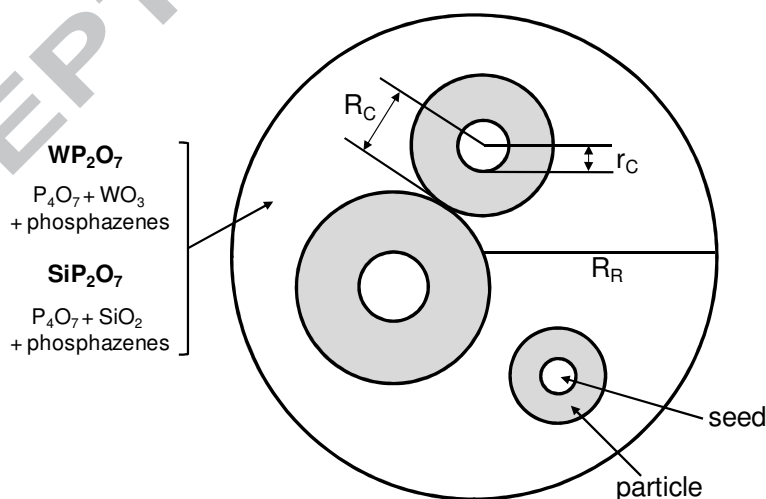


Figure 10 Schematic model of a region of the pyrolyzed precursor in which nanoparticles are seeded and grow through crystallization. R_R is the radius of the region of interest (assumed circular in the analysis) composed of the reactants and the host material of P_4O_7 and less than fully carbonized phosphazenes. The radius r_C of the seed particles as determined from HRTEM, and R_C is the final radius of a nanoparticle up to the point of contact with another nanoparticle or crystalline region.

The seeds are given a definitive radius $r_C = 1$ nm and a critical radius $R_C = 4$ nm. Crystallization is assumed to occur both outward into the host and inward into the particle, before $r_C = R_C$ at which point crystallization is halted. The approach is general and no assumption is made on whether crystallization occurs from the center of the particular outwards only, since it is known that inward crystallization can also occur. At radii below and above $r_C = R_C$, the volume fraction of crystallization must therefore be different. The growth of crystalline nuclei is calculated based on the model developed by Prado and Zanotto⁴². Their model discussed crystallization on the surface of a particle; here it is used to describe the crystallization of the seeds within a larger ‘particle’, a spherical region of the host-particle composite. The growth of the seed is described by

$$r_c(t) = \int U(t) dt$$


where U is an Arrhenius-type crystal growth rate given by $U(T) = U_0 e^{-Q_c/RT}$. The volume fraction of the crystallized material $\delta_v(t)$ can be written^[42]

$$\delta_v(t) = (\delta_v^f - \delta_v^i) [1 - e^{-\pi R^3 / R_C^3}] + \delta_v^i \quad (1)$$

for $r_C \leq R_C$. Here, δ_v^f and δ_v^i are the final and initial volume fractions of crystallization. This describes the volumetric fraction of the seeds up to the final nanoparticle size after pyrolysis, such as the WP_2O_7 and TiO_2 particles reported here for example. Since the embedded nanoparticles are experimentally observed to stop further growth after forming a sphere, Eq. 1 is a valid description of their crystallization up to and including (in some cases) necking of two close particles (see. Figs 4e,f for example). For the *in situ* formation of SiP_2O_7 , we observe that coalescence of crystalline regions can occur, due to reaction with remnant phosphazenes. This adds to the already formed SiP_2O_7 crystal content in the host. In such cases, voids in the amorphous host are found as mentioned earlier. In this case, the crystalline volumetric fraction must consider the touching/merging of nanocrystalline particles as they grow, i.e. for $r_C \geq R_C$. This relationship is given by

$$\delta_v(t) = (\delta_v^f - \delta_v^i) [1 - e^{-\pi R^3 / R_C^3}] + \delta_v^f \quad (2)$$

where δ_v^f is the volume fraction when $r_C = R_C$. In the early stages (Eq. 1), the seeds grow and eventually form spherical nanoparticles. From Fig. 8 we observe that necking or coalescence of large and small nanoparticles

can occur to form a larger crystalline region and can be described by Eq. 2. Halting of further crystallization depends on the amount of reactants available in the amorphous host; what remains does not react and comprises the stabilizing P_4O_7 . This limiting situation describes what is observed; crystalline regions formed and merge until they come in contact, but do not sinter. This is represented by . Thus, the geometrical model helps explain the temporal crystallization within the host by considering the growth of particle seeds into particles and also in cases where continual crystallization causes merging of these regions as observed for *in situ* SiP_2O_7 formation.

In summary, WO_3 , TiO_2 and SiO_2 nanoparticles can be synthesized through a solid state route involving pyrolysis of organometallic derivatives of cyclotriphosphazenes. The type of nanoparticle formed can be controlled and, in addition, the rational synthesis of SiP_2O_7 and WP_2O_7 nanoparticles represents a new route to oxide and phosphate nanoparticles embedded in a host. Thus far, these materials are unreported in nanoparticulate form. Obtaining these nanostructured materials using organometallic derivatives of phosphazenes containing metal centers^[43] is a potentially useful route to a range of other nanostructured oxide and phosphate single crystal nanomaterials from transition and valve metals, particularly where non-stoichiometric phases and pyrophosphate formation is required. It constitutes a novel route to oxide and phosphate phases (at least) of multimetallic nanoparticles with potential applications ranging from interconnect metal deposition, high density surface functionalization with noble metal nanoparticles for nanocrystal embedded dielectrics, nanoparticle automotive catalysts^[44,45], surface-enhanced Raman scattering (SERS) and high lithium mobility phosphate cathode materials.^[25] Further work will investigate novel nanoparticle-containing layers with tunable particle density, size and phase selectivity on their surfaces.

4. Conclusions

We have presented a new solid-state synthetic strategy to prepare, in a one-pot synthesis, embedded nanoparticles of metal oxides and metal phosphates in a host matrix. Single-crystal nanoparticles and nanocrystals of SiP_2O_7 , SiO_2 , WP_2O_7 , TiO_2 and P_4O_7 are reported from newly synthesized heterobimetallic Si – Ti and Si – W-containing precursors formed by pyrolysis of their organometallic derivatives of

cyclotriphosphazenes. High-resolution transmission electron microscopy and related techniques have shown that the method allows reproducible synthesis of 2 – 6 nm particles of SiP_2O_7 and WP_2O_7 , which are the first reported rational synthesis of nanoscale crystals of these materials. Single crystal nanoparticles of SiP_2O_7 are formed *in situ* by electron beam-induced reaction of between the SiO_2 and unreacted precursor and linked to heating effects caused by electron bombardment of the amorphous pyrolytic product. This nano-reaction is observed for these compounds for the first time.

Crystallization processes are governed by the thermodynamics of amorphous recrystallization, where for WP_2O_7 nanocrystals, the amorphous host ensures individual particle formation and stabilization by excess P_4O_7 , while for SiP_2O_7 , sintering or densification crystallization occurs with voids formed in the host material as SiO_2 is consumed during the heat-induced reaction. The crystallization is dependent on the surrounding amorphous host and recrystallization occurs for WP_2O_7 and SiP_2O_7 at temperatures that are 0.72 and 0.64 of their respective bulk melting temperatures. Some of the advantages of this method in preparing metallic, oxidic, and semiconducting nanostructures in the solid-state are the synthetic simplicity in the preparation of the precursor (compared with analogous polymers for instance), the possibility of uniform distribution of the inorganic metal atom at the molecular level by the formation of a cyclomatrix network that acts as the template for the growth of the nanoparticles and embedded nanoparticle composites; mesoporous solids are obtained on the macroscale, with nanoparticle formation occurring within this phase, *i.e.* nanoparticle recrystallization within the inorganic solid host due to the mechanism of pyrolysis of the cyclophosphazene derivative. Thus the cyclomatrix is a useful host for the solid-state stabilization of individual nanoparticles of SiP_2O_7 , SiO_2 , WP_2O_7 , TiO_2 and P_4O_7 .

The method is also the first solid-state organometallic approach that allows successful formation of embedded nanoparticle containing host-guest nanocomposites. The approach can easily be extended to nearly all valve and transition metals capable of successful coordination as an organometallic. Embedded nanoparticle composites could be deposited as films (particularly for applications sensitive to moisture/solutions) and thermally treated to convert the film into a metal oxide or metal phosphate nanoparticle-containing layer for a variety of uses.

Acknowledgements

Financial support from FONDECYT Grant No. 1085011 is acknowledged. Part of this work was conducted under the framework of the INSPIRE programme, funded by the Irish Government's Programme for Research in Third Level Institutions, Cycle 4, National Development Plan 2007-2013.

Supporting Information Available

Details of the synthesis of the model precursors (4) – (7), characterization and analysis of the model precursors, HRTEM, SEM, EDX, IR, XRD and optical microscopy analysis of each precursor and pyrolytic product.

References

- [1] K. Klabunde and R. S. Mulukutla in *Nanoscale Materials in Chemistry*, Ed. K. Klabunde, John Wiley & Sons, New York, 2001, ch. 7, pp. 223.
- [2] *Nanoparticle and Nanostructured Films*, ed. J. H. Fendler, Wiley-VCH, Weinheim, 1998.
- [3] J. M. Buriak, *Science* 304 (2004)692.
- [4] R.-K. Chiang, R.-T. Chiang, *Inorg. Chem.* 46 (2007)369.
- [5] M. Niederberger, G. Garnweitner, *Chem. Eur. J.* 12 (2006)7282.
- [6] J. L. G. Fierro, L. L. G. Fierro, *Metal Oxides: Chemistry and Applications*, Taylor & Francis, CRC, Boca Raton, 2006.
- [7] M. L. Kahn, A. Glaria, C. Pages, M. Monge, L. Saint Macary, A. Maisonnat, B. Chaudret, *J. Mater. Chem.* 19 (2009)4044.
- [8] J. Y. Lao, J. Y. Huang, D. Z. Wang and Z. F. Ren, *Nano Lett.* 3, 2003, 235; J. Y. Lao, J. G. Wen and Z. F. Ren, *Nano Lett.* 2 (2002)1287.
- [9] Ch. Pan, K. Pelzer, K. Philippot, B. Chaudret, F. Dassenoy, P. Lecante, M.-J. Casanove, *J. Am. Chem. Soc.* 123 (2001)7584; N. Cordente, M. Respaud, F. Senecq, M. J. Casanove, C. Amiens, B. Chaudret, *Nano Lett.* 1 (2001)565; E. Ramirez, L. Erades, K. Philippot, P. Lecante, B. Chaudret, *Adv. Funct. Mater.* 17 (2007)2219.
- [10] R. D. Riecke, R. M. Wehmeyer, T. C. Wu and G. W. Eber, *Tetrahedron* 45 (1989)443.

- [11] D. J. Trevor, D. M. Cox, A. Kaldor, *J. Am. Chem. Soc.* 112 (1990)3742.
- [12] K. Soulantica, A. Maisonnat, F. Senocq, M.-C. Fromen, M.-J. Casanove and B. Chaudret, *Angew. Chem. Int. Ed.* 40 (2001)2983.
- [13] Roy, R.; Agrawal, D. K.; McKinsty, H. A., *Annu. Rev. Mater. Sci.* 19 (1989)59; A. W. Sleight, *Annu. Rev. Mater. Sci.* 28 (1998)29.
- [14] L. D. Marks, *Rep. Prog. Phys.* 57 (1994)603; J. Zhu, T. Sun, H. Hoon Hng, J. Ma, F.Y. Chiang Boey, X. Lou, H. Zhan, C. Xue, H. Chen, Q. Yan, *Chem. Mater.* 21 (2009) 3848.
- [15] S. Sepulveda, N. Villareal, D. Ferrer, A. Torres, X. Gao, J. P. Zhou, M. J. Yacaman *Nanotechnology* 18 (2007)335604; I. S. Molcahn, G. E. Thompson, P. Skeldo, R. Andriessen, J. *Colloid Interface Sci.* 323 (2009)282; O. Van Overschelde, G. Guisbiers and M. Wautelet, J. *Phys. Chem. C* 113 (2009)15343.
- [16] R. Diaz-Ayala, E. R. Fachini, R. Raptis, C. R. Cabrera, *Langmuir* 22 (2006)10185; Ch. Li, Z. Zhong, W. K. Leong, *Langmuir* 24 (2008)10427.
- [17] A. L. Schmitt, M. J. Bierman, D. Schmeisser, F. J. Himpsel, S. Jin, *Nano. Lett.* 8 (2006)1617.
- [18] M. N. McCain, S. Schneider, M. R. Salata, T. J. Marks, *Inorg. Chem.* 47 (2008)2534; C. Pan, K. Pelzer, K. Philippot, B. Chaudret, F. Dassenoy, P. Lecante, J. M. Casanove, *J. Am. Chem. Soc.* 123 (2001)7584.
- [19] D. Wostek-Wojciechowska, J. K. Jeska, C. Amiens, B. Chaudret, P. Lecante, *J. ColloidInterface Sci.* 287 (2005)107.
- [20] O. Carp, L. Patron, A. Reller, *Mater. Chem. Phys.* 101 (2007)142.
- [21] C. Diaz, M. L. Valenzuela, D. Bravo, V. Lavayen, C. O'Dwyer, *Inorg. Chem.* 47 (2008)11561; C. Diaz, M. L. Valenzuela, A. Laguna, V. Lavayen, J. Jimenez, L. A. Power, C. O'Dwyer, *Langmuir* 26 (2010)10223; J. Jiménez, A. Laguna, J. A. Sanz, C. Díaz, M. L. Valenzuela, P. G. Jones, *Chem. Eur. J.* 15 (2009)13509.
- [22] a) C. Díaz, P. Castillo and M. L. Valenzuela, *J. Cluster Sci.* 16 (2005)515; b) C. Díaz, M. L. Valenzuela, E. Spodine, Y. Moreno O. Peña. *J. Cluster Sci.* 18(2007)831;c) C. Díaz, M. L. Valenzuela, S. Ushak, *J. Cluster Sci.* 19(2008)471; d) C. Díaz, M. L. Valenzuela,

Macromolecules 39(2006)103; e) C. Díaz and M. L. Valenzuela, J. Inorg. Organomet. Polym. 16

(2006)123; f) C. Díaz and M. L. Valenzuela, J. Inorg. Organomet. Polym. 16 (2006)419.

- [23] C. Díaz, M. L. Valenzuela and L. Zuñiga, C. O'Dwyer, J. Inorg. Organomet. Polym. 19 (2009)507.
- [24] P. I. Richards and A. Steiner, Inorg. Chem. 43 (2004)2810; E. W. Ainscough, A. M. Brodie, C. V. Craig Depree, G. B. Jameson and C. A. Otter, Inorg. Chem. 44 (2005)7325; E. W. Ainscough, A. M. Brodie, R. J. Davidson and C. A. Otter, Inorg. Chem. Commun. 11 (2008)171; O. S. Jung, Y. T. Kim, Y. A. Lee, Y. J. Kim, H. K. Chae, Inorg. Chem. 38 (1999)5457; B. Chandrasekhar, B. Murugesu, R. Azhakar, Inorg. Chem. 45 (2006)3510; C. Diaz, V. Lavayen, and C. O'Dwyer, J. Solid-State Chem. 183 (2010) 1595.
- [25] L. Taberna, S. Mitra, P. Poizot, P. Simon, J. M. Tarascon, Nat. Mater. 5 (2006) 567; K. S. Kang, Y. S. Meng, J. Breger, C. P. Grey, G. Ceder, Science 311 (2006) 977; B. Kang, G. Ceder, Nature 458 (2009) 190.
- [26] V. Chandrasekhar, S. Nagendran, Chem. Soc. Rev. 193 (2001)21; V. Chandrasekhar, in Inorganic and Organometallic Polymers, Springer, New York, 2004.
- [27] M. Gleria, R. De Jaeger in Applicative Aspects of Cyclotriphosphazenes, Nova Science Publishers, New York, 2004.
- [28] T. J. Barton, L. M. Bull, W. G. Klemperer, D. A. Loy, B. McEnaney, M. Misono, P. A. Monson G. Pez, G. W. Scherer, J. C. Vartuli, O. M. Yaghi, Chem. Mater. 11 (1999)2633; C. T. Kresge, M. E. Leonowicks, W. G. Roth, J. C. Vartuli, J. S. Beck, Nature 359 (1992)710.
- [29] N. Shibata, M. Horiguchi, T. Edahiro, J. Non-Crystalline Solids 45 (1981)115; J. Wong, J. Non-Crystalline Solids 20 (1973)83.
- [30] D. J. Hook, T. G. Vargo, J. A. Gardella, K. S. Litwiler, V. Bright, Langmuir 7(1991)142.
- [31] S. Bakardjieva, V. Stengl, L. Szatmary, J. Subrt, J. Lukac, N. Murafa, D. Niznansky, K. Cizek, J. Jirkovsky and N. Petrova, Chem. Mater. 16 (2006)1709.
- [32] V. V. Lisnyak, N. V. Stus, N. S. Slobodyanik, N. M. Belyavina, V. Ya. Markiv, J. Alloys and Compounds 309 (2000)83.
- [33] H. Hofmeister, J. Dutta, H. Hofmann, Phys. Rev. B 54 (1996)2856.

- [34] D. M. Poojaray, R. B. Borade, A. Clearfield, *Inorg. Chim. Acta.* 208(1993)2; D. M. Poojaray, R. B. Borade, F. L. Campbel, A. Clearfield, *J. Solid State Chem.* 112(1994)106; G. A. Carriedo, F. J. Alonso, C. Diaz, M. L. Valenzuela, *Polyhedron* 25 (2006)105.
- [35] N. Nishiyama, J. Kaihara, Y. Nishiyama, Y. Egashira, K. Ueyama, *Langmuir* 23 (2007)4746.
- [36] V. Kovalchuk, H. Sfihi, A. S. Korchev, A. S. Kovalenko, G. Il'in, V. N. Zaitzev, J. Fraissard, *J. Phys. Chem.* 109(2005)13948.
- [37] C. Díaz, M. L. Valenzuela, N. Yutronic, *J. Inorg. Organomet. Polym.* 76 (2007)577.
- [38] F. G. Shi, *J. Mater. Res.* 9 (1994)1307.
- [39] S. Veprek, Z. Iqbal, F. A. Sarott, *Phil. Mag. B* 45 (1995)137.
- [40] K. Lu, *Phys. Rev. B* 51 (1995)18.
- [41] I. Gutzow, R. Pascova, A. Karamanov, *J. Mater. Sci.* 33 (1998)5265.
- [42] M. O. Prado, E. D. Zanotto, *Comptes Rendus Chimie* 5 (2002)773.
- [43] C. Díaz, M. L. Valenzuela, S. Ushak, V. Lavayen, C. O'Dwyer, *J. Nanosci. Nanotechnol.* 9 (2009) 1825.
- [44] M. Corbiere, J. Beerens, R. B. Lennox, *Chem. Mater.* 17 (2005)5774.
- [45] A. T. Bell, *Science* 299 (2003) 1688.

- First derivatives of cyclic phosphazenes containing two metals in non-geminal positions.
- Electron beam writing of nanoparticles within an amorphous host and first demonstration of embedded nanoparticle formation in the solid state.
- Growth mechanism of twinned nanocrystals of the negative thermal expansion material WP_2O_7 .
- Stabilizing role of P_4O_7 during crystallization of embedded nanoparticles in oxide host.
- Model of sintering-based recrystallization to explain embedded nanoparticle formation in host-guest systems where a solid forms within a solid.

